**Showcasing research from the Energy, Environment and Sustainability Laboratory / Nano Fabrication Laboratory, Seoul National University, Seoul, Republic of Korea.**

Sub-10 nm transparent all-around-gated ambipolar ionic field effect transistor

A versatile ionic field effect transistor (IFET) which has an ambipolar function for manipulating molecules regardless of their polarity was developed for the operation at a wide range of electrolytic concentrations (10^{-5} M–1 M).
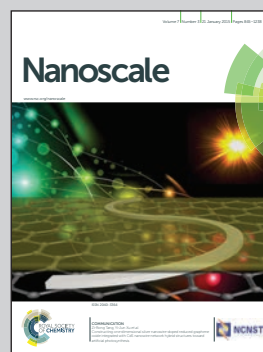
ROYAL SOCIETY
OF CHEMISTRY

www.rsc.org/nanoscale

Sub-10 nm transparent all-around-gated ambipolar ionic field effect transistor†

Seung-Hyun Lee,‡[a] Hyomin Lee,‡[b,c] Tianguang Jin,[a] Sungmin Park,[b] Byung Jun Yoon,[c] Gun Yong Sung,[d] Ki-Bum Kim*[a] and Sung Jae Kim*[b]

In this paper, we developed a versatile ionic field effect transistor (IFET) which has an ambipolar function for manipulating molecules regardless of their polarity and can be operated at a wide range of electrolytic concentrations (10^{-5} M–1 M). The IFET has circular nanochannels radially covered by gate electrodes, called "*all-around-gate*", with an aluminum oxide (Al_2O_3) oxide layer of a near-zero surface charge. Experimental and numerical validations were conducted for characterizing the IFET. We found that the versatility originated from the zero-charge density of the oxide layer and all-around-gate structure which increased the efficiency of the gate effect 5 times higher than a previously developed planar-gate by capacitance calculations. Our numerical model adapted Poisson–Nernst–Planck–Stokes (PNPS) formulations with additional nonlinear constraints of a fringing field effect and a counter-ion condensation and the experimental and numerical results were well matched. The device can control the transportation of ions at concentrations up to 1 M electrolyte which resembles a backflow of a shale gas extraction process. Furthermore, while traditional IFETs can manipulate either positively or negatively charged species depending on the inherently large surface charge of oxide layer, the presenting device and mechanism provide effective means to control the motion of both negatively and positively charged molecules which is important in biomolecule transport through nanochannels, medical diagnosis system and point-of-care system, *etc.*

Introduction

Recent advances in nano-fabrication methods enable the fabrication of rigorous and definite nano-sized structures for various scientific and engineering applications. Nanostructures possess unique scientific and technological properties that microstructures cannot exhibit, especially since decreasing the size of nanostructures below 100 nm, the structures have a perm-selectivity which let only counter-ions pass through below a critical electrolyte concentration. The perm-selectivity was reported to be dependent on the magnitude and polarity of surface charge density and bulk electrolyte concentration. Thus, the active control of the surface charge density at a wide range of electrolyte concentrations has drawn significant attention in both the scientific and engineering fields[1–6] for manipulating the motion of charged species,

which has become one of the important fields in nanofluidics research. The emerging fields of application of nanofluidic systems are energy harvesting,[1,2] biosensors,[3,4] backflow from shale gas extraction ports[5] or desalination of seawater[6] which will enable the creation of a huge market that never existed before. Those applications were fundamentally originated from controlling the motion of charged species passing through a nanostructure and therefore, the cost-effective/on-demand/sensitive control has become the most important practical issue of nanofluidic research.

Various passive types of modulating the motion of a charged species in nanofluidic systems were reported such as changing the viscosity of the solution in the nanochannel,[7] utilizing mechanical friction between DNA and the nanopore,[8] coating an adhesive material on the nanochannel[9] and surface treatment for changing the surface potential.[10,11] Those platforms employed passive methods which were unable to change the behavior of charged species on-demand, once the devices were fabricated. In contrast, IFET can provide an active method which enables it to enhance, diminish or even reverse the behavior of charged species *in situ* by introducing gate potential. However, traditional IFETs can manipulate either positively or negatively charged species depending on the inherently large surface charge of the oxide layer and they demand either high gate voltage or low electrolyte concentration for changing

ᵃDepartment of Materials Science and Engineering, Seoul National University, Korea. E-mail: kibum@snu.ac.kr
ᵇDepartment of Electrical and Computer Engineering, Seoul National University, Korea. E-mail: gates@snu.ac.kr
ᶜDepartment of Chemical Engineering, POSTECH, Korea
ᵈDepartment of Materials Science and Engineering, Hallym University, Korea
†Electronic supplementary information (ESI) available. See DOI: 10.1039/c4nr04089a
‡Those authors contributed equally.

surface charge density.[11–16] Traditional fabrication of IFET was principally by using SiO_2[11–13,15,16] and a nanoporous membrane.[14,17,18] While they had easy-fabrication and relatively high uniformity, these materials had high surface charge density which led to a unipolar behavior.[11–16] The reason why the unipolar behavior occurs is that induced surface potential by gate voltage cannot overcome a polarity of inherent surface potential. Due to this characteristic, a traditional IFET can only control the same polarity of charged species with the surface charge of the nanochannel. Additionally, in a planar gate structure in which a gate electrode is installed, only one wall of the nanochannel can modulate the surface charge density at the wall and thus, the efficiency of applying gate voltage would become lower than an all-around-gate structure which had a gate electrode at the entire surface of the nanochannels. Therefore, as previously suggested, "*an ideal structure for field effect reconfigurable nanofluidic diodes would be dual split-gates with a gate-all-around structure and a sub-10 nm nanochannel of a neutral surface.*"[16,19] In this work, we have developed a novel design of all-around-gate structure, with 7.5 nm radius nanochannels and minimal surface charge

density using Al_2O_3, which has the surface charge density of -1.5 mC m^{-2}. Firstly, an all-around-gate structure was adapted to increase the efficiency of the gate effect at least more than 5 times compared to planar-gate structure. This high efficiency led to an ionic field effect at high electrolyte concentration up to 1 M. Secondly, we deposited Al_2O_3 which has low surface charge density for enabling a polarity independent control. As a result, our device showed an ambipolar behavior at I_D–V_G measurement. The experimental ambipolar effects were validated by numerical simulations with a fringing field effect and a counter-ion condensation which had not been considered as major factors. The experimental and numerical results were in line with our logical procedures and well-matched.

Materials and methods

While the all-around-gated IFET device was fabricated based on a previously reported method,[20,21] advanced features such as transparency were upgraded in this work and its fabrication process is summarized in Fig. 1(a). A detailed description can
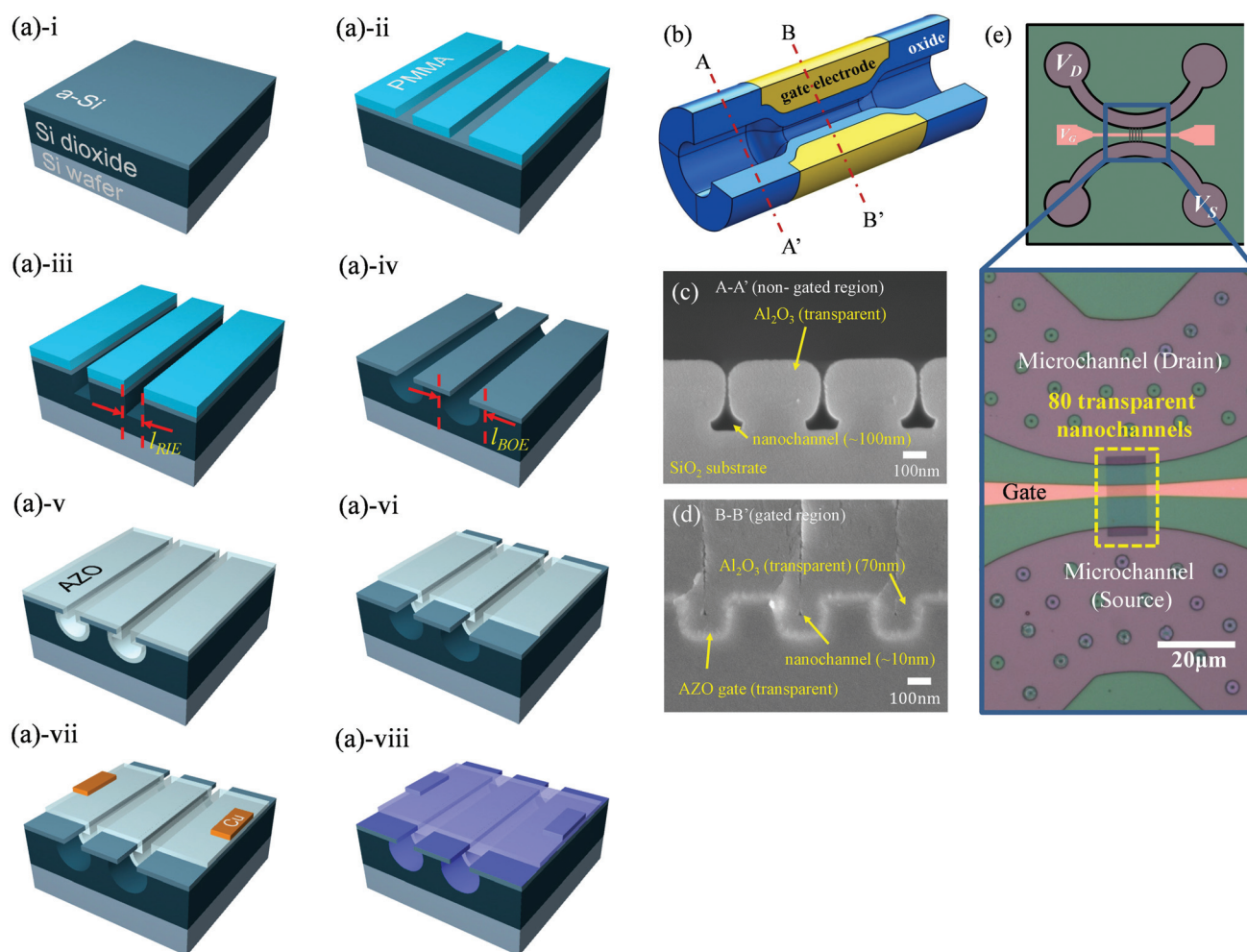

Fig. 1 (a) Schematics of the fabrication process. (b) The schematic diagram of all-around-gated IFET. Cross-sectional SEM images of (c) non-gated region and (d) gated region. (e) Microscopic image of IFET device near nanochannel array.

be found in ESI.† Fig. 1(b) showed schematics of fabricated nanochannel. The nanochannel had a constricted area in the middle because a gate electrode existed only at the center of nanochannel. Fig. 1(c) and 1(d) showed the SEM image of the cross section of non-gated region (~100 nm opening) and gated region (~10 nm opening). Fig. 1(e) showed the assembly device with magnified microscopic view near the nanochannel. Note that the color of AZO electrode (a pink color) could be observed through nanochannel array so that we confirmed the nanochannels in this work had an optical transparency. We measured the ionic current (I_D) for different gate voltages (V_G) with KCl buffer solution at pH 7 in the concentration range from 10^{-5} M to 1 M. The fluidic chambers were covered with PDMS and Ag/AgCl electrodes were connected on both sides of the chambers. In order to infiltrate water into the thin nanochannel, oxygen plasma was treated to enhance hydrophilicity[19] and ethanol was filled first and then it was replaced by water to ensure wetting. We measured the electric data using the parameter analyzer (Agilent 4156C) in the homemade dark box which blocked the electrical noise. The current was measured as follows. First, drain voltage (V_D) increased from 0 V to +2 V at 0.25 V min^{-1} for low concentration and 0.5 V min^{-1} for high concentration, respectively. After a 5 min delay time, V_D decreased from 0 V to −2 V at the same voltage step. For each concentration of KCl, the microchannel was refreshed for 10 minutes with the same solution using a rotary pump. The measurements without the application of gate voltage were repeated until the results were reproduced. For a high concentration case such as 10^{-1} M and 1 M, serious precipitation occurred inside the microchannels. To prevent it, we added a refresh step at each change of gate voltage. Leakage current (a current from source to gate) was simultaneously measured for confirming the proper operation.

Numerical scheme

Domain definition

The numerical domain to describe the ion transport through the IFET is depicted in Fig. 2. To reduce computational cost, we simulated for single channel and then, multiplied the
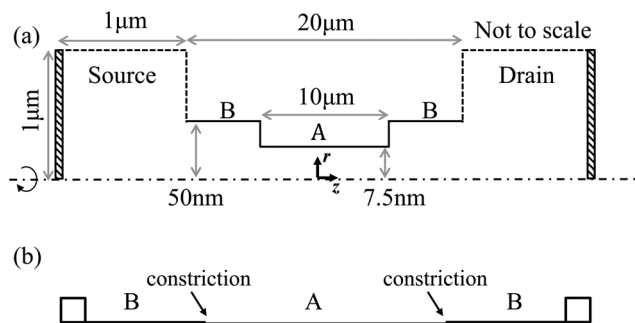

Fig. 2 (a) Schematic representation of numerical domain (not to scale). A and B denote the non-gated and gated regions respectively. (b) The actual numerical domain.

number of fabricated nanochannels and each numerical quantity to compare with the experimental results. A cylindrical coordinate system was adopted for the circular cross-sectional nanochannel. The gate electrode and the oxide layer were omitted in our numerical domain, but they affected the boundary conditions of the electrokinetic system. Thus, the empty space of the gate electrode played as a geometrical constriction. The constriction of the nanochannel positioned near the center of the channel (denoted as A) had 10 μm length and 7.5 nm radius. The rest of the nanochannel (denoted as B) had 5 μm length and 50 nm radius, so that the total length of the nanochannel was 20 μm. Source and drain reservoirs were connected at the left and right side of the nanochannel, respectively. Note that the schematic in Fig. 2(a) was exaggerated in aspect ratio and the actual domain was shown in Fig. 2(b). Although the reservoir dimensions should be larger than the length of the nanochannel for the consideration of the entrance effect inside the reservoirs,[22] our 1 μm reservoirs were enough to simulate the system regardless of the entrance effect by obtaining similar results with the reservoir size of 1 μm, 5 μm and 20 μm. This was because major variations in electrokinetic quantities occurred near the gate electrode. Governing equations for describing the gate modulation such as the Poisson–Boltzmann equation and the Laplace equation were independently solved as similar to literature,[23–26] so that the number of degrees of freedom could be reduced remarkably. The detailed Poisson–Nernst–Planck–Stokes formulation and proper boundary conditions are shown in ESI.†

General description for metal-oxide-electrolyte (MOE) system

In the usual MOE system, the surface charge density is obtained from simple algebraic equations independent of governing equations. In various literature,[23–26] the MOE system was approximated to series capacitors by equivalent electrokinetic circuit models. Using those models, zeta potential and surface charge density modulated by gate voltage can be analyzed by solving simple algebraic equations. However, those equations are only valid in the planar-type MOE system. Therefore, those models should be reformulated to be applicable to the cylindrical MOE system, which is our system. When the Stern layer and the chemistry of oxide/electrolyte interface are neglected,[25,27] the charging behavior of the MOE system can be described by the following set of 1D ordinary differential equations based on Gouy-Chapmann theory in case of symmetric electrolyte.

$$\frac{1}{r}\frac{d}{dr}\left(r\frac{d\phi}{dr}\right) = \frac{2ZFc_0}{\varepsilon_f}\sinh\left(\frac{ZF\phi}{RT}\right) \quad \text{at } 0 < r < R_f, \quad (1)$$

and

$$\frac{1}{r}\frac{d}{dr}\left(r\frac{d\Phi}{dr}\right) = 0 \quad \text{at } R_f < r < R_f + d_{ox}. \quad (2)$$

In the above, ϕ is the electric potential in the electrolyte, Φ is the electric potential in the oxide layer, c_0 is the bulk con-

centration, F is the Faraday constant, ε_f is the electrical permittivity of the electrolyte, R_f is the radius of the nanofluidic channel, d_{ox} is the oxide layer thickness, and Z is ion valence. Eqn (1) is the Poisson–Boltzmann equation expressed as cylindrical form to describe the potential distribution inside the nanochannel and eqn (2) is the Laplace equation describing the potential distribution within the oxide layer. Because we neglect the Stern layer, zeta potential is approximately equal to surface potential, $\zeta = \varphi|_{R_f}$, directly given by gate voltage, V_G. Thus, the modulated zeta potential corresponding to V_G can be obtained by solving eqn (1) and (2) with the following boundary conditions.

$$\frac{d\phi}{dr} = 0 \quad \text{at } r = 0, \tag{3}$$

$$\varphi = \Phi \quad \text{at } r = R_f, \tag{4}$$

$$-\varepsilon_f \frac{d\phi}{dr} + \varepsilon_{ox} \frac{d\Phi}{dr} = \sigma_0 \quad \text{at } r = R_f, \tag{5}$$

and

$$\Phi = V_G \quad \text{at } r = R_f + d_{ox}, \tag{6}$$

where ε_{ox} is the electrical permittivity of the oxide layer and σ_0 is the inherent surface charge density on oxide/electrolyte interface which is near-zero value in our ambipolar IFET system, while the typical value of σ_0 is high enough to have unipolar electrical response.[12,13] Eqn (3) is the condition for axis of symmetry, eqn (4) and (5) describe oxide/electrolyte interface, and eqn (6) is the voltage condition by gate electrode. eqn (5) implies the discontinuity of electric displacement field at the interface where Gauss's law for electrostatic field should be satisfied. Since the above formulation is valid to a system where the full length of the nanochannel is completely covered by a gate electrode with low gate voltage (fully-gated IFET), we need additional considerations for the partial coverage of the gate electrode (partially-gated IFET) as shown in Fig. 2(a) with high gate voltage. The considerations are a fringing field effect and a counter-ion condensation as follows.

Fringing field effect

Despite the difference in structure, the zeta potential modulation of partially-gated IFET could be similar to that of fully-gated IFET, in physical intuition. Here, we define 'gated region' as a region of gate electrodes and 'non-gated region' as a region of absence of gate electrodes. Gated and non-gated regions correspond to 'A' and 'B' denoted in Fig. 2(a), respectively. Typically, when voltage is applied to the gate electrode, the electric field is thought to be generated only inside the oxide layer of the gated region and the electric field abruptly drops to zero in that of non-gated region. However, this is impossible because of the conservative nature of the electric field, $\nabla \times \mathbf{E} = \mathbf{0}$.[28] To satisfy the conservation, the electric field should curve and extend outward into the non-gated region which is called the fringing field effect or edge effect. Due to this fringing field, the zeta potential on oxide/electrolyte interface of the non-gated region can be modulated as similar to

the gated region. The impact of fringing field was researched by Lin *et al.*,[29] using carbon nanotube FET (CNFET) where fringing field affected the gating phenomena significantly. To solve fringing field directly, it requires high-cost computation. Numerical domain must be discretized into nearly zero sized elements in the vicinity of each gate end, so that the number of degrees of freedom diverges. To avoid this, we assumed that the distribution of the modulated zeta potential along the nanochannel wall followed the Gaussian distribution expressed as

$$f(x) = \frac{A}{\sigma\sqrt{2\pi}} \exp\left[-\frac{(x-\mu)^2}{2\sigma^2}\right] \tag{7}$$

where A is an arbitrary constant, σ is the standard deviation, and μ is the mean value of the arbitrary function $f(x)$, respectively. Using eqn (7), the modulated zeta potential along the channel walls was set to be

$$\zeta(z) = \begin{cases} \zeta_{gate} \exp\left[-\frac{\left(z+\frac{L_{gate}}{2}\right)^2}{\alpha^2}\right] & \text{at} \quad z < -\frac{L_{gate}}{2}\,(\text{region B}) \\[4mm] \zeta_{gate} & \text{at} \quad -\frac{L_{gate}}{2} \leq z \leq \frac{L_{gate}}{2}\,(\text{region A}) \\[4mm] \zeta_{gate} \exp\left[-\frac{\left(z-\frac{L_{gate}}{2}\right)^2}{\alpha^2}\right] & \text{at} \quad z > \frac{L_{gate}}{2}\,(\text{region B}) \end{cases} \tag{8}$$

In the above expressions, ζ_{gate} is the modulated zeta potential on the oxide/electrolyte interface by the gate electrode which is calculated from eqn (1)–(6). α^2 is defined as $\alpha^2 = (L_{channel} - L_{gate})^2/4\ln\beta$ in which $L_{channel}$ is the length of the nanochannel, L_{gate} is the length of the gated region and $\beta = \zeta_{gate}/\zeta_{min}$ is the ratio of the modulated zeta potential and its minimum zeta potential at the end of the nanochannel wall. Since β is a phenomenological parameter, one can choose it in the range of 1 to ∞. For example, of the limiting cases, β is equal to 1, corresponding to fully-gated system and β goes to infinity, diminishing the fringing field effect. We postulated that β is proportional to the electrical conductivity of the electrolyte solution and its values are summarized in ESI Table 2.†

Counter-ion condensation

Surface charge density, σ_s in ESI Table 1† can be determined from the modulated zeta potential if charge-potential relation in the electrokinetic system is known. In the classical viewpoint, the Grahame equation based on the Poisson–Boltzmann equation can be used to determine the surface charge density. However, when the zeta potential exceeds the thermal voltage, $RT/F \approx 25$ mV, the electric double layer starts to enter a nonlinear regime where the Grahame equation is expected to break down.[23,30,31] Under the conditions such as high zeta potential or high electrolyte concentration, one should consider the ion–ion interactions so that surface charge overscreening and ion crowding are in the vicinity of the solid/electrolyte interfaces. To elucidate those non-linear effects, additional compact layer consisting of counter-ions has been

proposed.[30,32] In the literature, counter-ions in the vicinity of the highly charged surface are condensed in a narrow layer, and then a new compact layer is formed beyond the Stern layer. Consequently, the impact of the highly charged surface to the electric double layer structure is reduced by condensed counter-ions. To obtain charge-potential relation in that non-linear regime, Kilic and coworkers established the analytical model based on the modified Poisson–Boltzmann equation with a phenomenological parameter[30] which we chose in this work.

In their model, parameter ν represents the ratio of bulk electrolyte concentration (c_0) and maximum condensed concentration (c_{max}) expressed by

$$\nu = \frac{2c_0}{c_{max}} = 2a^3 N_A c_0 \qquad (9)$$

where N_A is the Avogadro number and a is the effective diameter of an ion. Note that a is not necessarily the actual diameter of an ion (the order of 1 angstrom); it just means ion–ion correlation under phenomenological viewpoint. By definition of (9), ν has a maximum value, 2 because c_0 cannot exceed the maximum concentration, c_{max}. By their theoretical derivation without the loss of generality, charge-potential relation has the following form,

$$\sigma_s = 2\text{sgn}(\zeta)ZFc_0\lambda_D \sqrt{\frac{2}{\nu}\ln\left[1 + 2\nu \, \sinh^2\left(\frac{ZF\zeta}{2RT}\right)\right]} \qquad (10)$$

where λ_D is the Debye layer thickness defined as $\lambda_D = \sqrt{(\varepsilon_f RT)/(2Z^2F^2c_0)}$, $\text{sgn}(\zeta)$ is the sign of the zeta potential, and ζ is calculated from eqn (8). The σ_s is used as the boundary conditions in ESI Table 1.† Due to highly confined nanostructure (radius in the order of 10 nm), ion–ion correlations were expected to be strong. To capture the strong correlation, the effective diameter of an ion, a, is fixed to be 7.5 nm,[30] so that ν is proportional to the bulk electrolyte concentration from eqn (9) of which values are summarized in ESI Table 2.†

Ionic current

To obtain theoretical I–V characteristics of IFET, local ionic current density, $\mathbf{i}$, is defined by

$$\mathbf{i} = \sum_j Z_j F\left(-D_j\nabla c_j - \frac{Z_j FD_j}{RT}c_j\nabla\psi + c_j\mathbf{u}\right) \qquad (11)$$

and then total ionic current through IFET system (I) can be calculated by

$$I = N_{ch}\int_S \mathbf{i}\cdot\mathbf{n}dS \qquad (12)$$

where N_{ch} is the number of nanochannel, S is arbitrary cross section of the system, and $\mathbf{n}$ is normal vector on surface S. Required field quantities in eqn (11) were obtained from eqn (1)–(10) with governing equations and boundary conditions shown in ESI.†

Results and discussion

Ionic conductance at floating gate

Ionic transport in nanofluidic systems have the unique property of surface-charge-governed regime as demonstrated by D. Stein et al.[10] In a dilute limit, ionic conductance is independent from the bulk properties of the system such as the electrolyte concentration or the geometrical factor, so that the conductance curve saturates below a specific concentration value which is determined by surface charge density and called 'surface-charge-governed conductance'. Because the plateau of the conductance curve is only revealed in a nano-channel system, this property has been utilized to demonstrate the validity of the device in the view point of nanofluidic application. Beyond the specific concentration value, the conductance is proportional to the bulk concentration, called geometry-governed regime. These two distinct regimes can be plotted (ionic conductance as a function of bulk concentrations) simultaneously as shown in Fig. 3. In a cylindrical nanochannel, the analytical expression of ionic conductance, G, was derived[33] as

$$G = \frac{\pi}{4}\frac{d_{nano}^2}{L_{nano}}\left[(\mu_{co} + \mu_{counter})c_0 F + \mu_{counter}\frac{4|\sigma_0|}{d_{pore}}\right] \qquad (13)$$

where d_{nano} is the diameter of a nanochannel, L_{nano} is the length of a nanochannel, and μ_{co} and $\mu_{counter}$ are the electrophoretic mobility of co- and counter-ions, respectively. The first term in eqn (13) represents the bulk conductance and the second term represents the surface-charge-governed conductance. Using eqn (13) and circuit theory, the total conductance
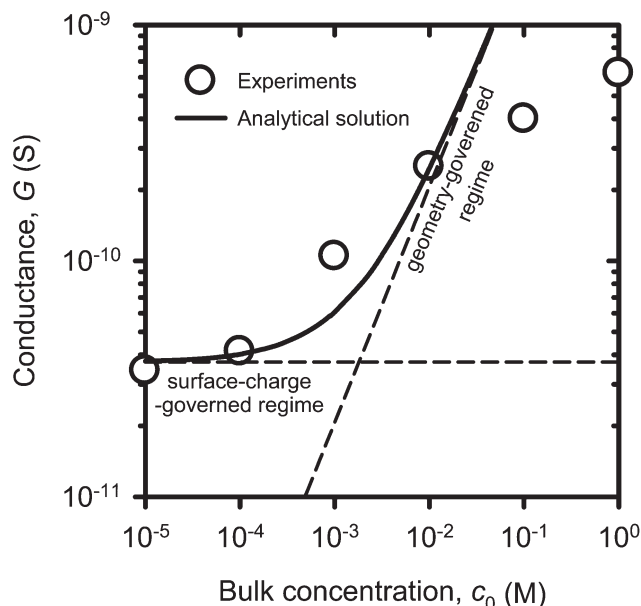

Fig. 3 Ionic conductance as a function of bulk concentration. Experimental conductance and analytical solutions are denoted by open circles and solid line, respectively. The plot clearly demonstrates a nanofluidic characteristic of surface-charge- and geometry-governed regime.

of our IFET at floating gate, G_{total}, was calculated from $G_{total} = 80 \times (G_{gated} \times G_{non\text{-}gated})/(2G_{gated} + G_{non\text{-}gated})$ in which G_{gated} and $G_{non\text{-}gated}$ are the ionic conductance of gated and non-gated regions, respectively. We used values of $\mu_{co} = 7.853 \times 10^{-8}$ m^2 V^{-1} s^{-1}, $\mu_{counter} = 7.582 \times 10^{-8}$ m^2 V^{-1} s^{-1}, $|\sigma_0| = 1.5$ mC m^{-2}, $d_{nano} = 15$ nm (gated region) and 100 nm (non-gated region), and $L_{nano} = 10$ μm (gated region) and 5 μm (non-gated region). Both theoretical (solid line) and experimental (circles) conductance as a function of bulk concentration are shown in Fig. 3. In a low concentration range ($c_0 < 10^{-4}$ M), experiments were saturated to the surface-charge-governed conductance and consistent with analytical solution and the conductance fell into the geometry-governed regime above the concentration. However, in a high concentration range, i.e. $c_0 > 10^{-1}$ M, the experiments deviated from the theoretical calculation, while previous literature followed the theoretical calculation over 1 M.[10,33,34] The discrepancy could be as a result of highly confined microchannels. Our microchannels had the thickness of 1.5 μm, while previous studies usually provided the demonstration with an open reservoir. The thin microchannel could provoke strong ion–ion interactions or ion–wall interactions in a high concentration range so that KCl solution at 10^{-1} M and 1 M concentration turned into a salt precipitate that hindered the ionic current through the micro-nanochannel since the precipitate acted as a physical obstacle (see the ESI† for the salt precipitate formation). In spite of the discrepancy at high concentration range, we concluded that our device was intact because surface-charge-governed conductance as the unique property of nanofluidic system was observed.

Ionic current with gate voltage

The ionic currents (I_D vs. V_D) were measured as a function of gate voltage (V_G) at the concentration range from 10^{-5} M to 1 M as shown in Fig. 4, demonstrating the ohmic (or linear) relationship between I_D and V_D within the voltage range of $|V_D| < 2$ V. Over the range, one can have ion concentration polarization phenomena which involve a non-linear current–voltage relationship.[35,36] At higher KCl concentration, we obtained higher ionic current values. Upon the application of gate voltage, ionic conductance increased regardless of the polarity of gate voltage for the entire concentration range, called ambipolar behavior. The terminology of 'ambipolar' in MOSFET (Metal-Oxide-Semiconductor Field-Effect Transistor) represents that the channel polarity strongly depends on the polarity of gate voltage. For instance, negative gate voltage induces abundant holes inside the channel, so that the channel demonstrates positive polarity and vice versa. In case of IFET, the same mechanism would hold with near-zero surface charge. Thus, the increment of ionic current was proportional to the absolute value of the gate voltage. On the contrary, the ionic current should increase with either positive or negative gate voltage, if the IFET had unipolar characteristics. The ambipolar behavior originated from the fact that the nanochannel had extremely low surface charge density due to the Al$_2$O$_3$ layer and the gate electrode had a so-called "all-around-gate structure" for the high sensitivity. The presenting

devices had two distinguishing features; (1) sub-10 nm channel size and (2) near-zero surface charge. The operation even at high electrolyte concentration would benefit from sub-10 nm channel size since thinner geometry retains stronger perm-selectivity.[6,10] The presenting high efficiency of gate modulation would be helped by the near-zero surface charge since the small change in gate voltage can be relatively large in the case of an extremely low surface charge.[13,14] In order to show the robustness of the system, we simultaneously measured the leakage current from source to gate. ESI Fig. 3† showed that the leakage currents were below 4 pA and independent of the bulk concentrations, leading to a judgment that the leakage current would not affect the ionic currents.

Electrokinetics of the ambipolar IFET

Because the IFET system involves a fluid with electricity, an analysis of electrokinetic fields such as electrostatic potential (ψ), averaged concentration distribution ($c_m \equiv (c_K + c_{Cl})/2$) and flow field (**u**) should be required for the characterization of the system. As we described in the numerical scheme section, those fields can be obtained by solving the coupled governing equations with the consideration of a fringing field effect and counter-ion condensation. Fig. 5–7 depict electrostatic potentials, concentration fields, and flow fields inside the ambipolar IFET at the bulk concentration of 10^{-3} M and the applied drain voltage of 2 V. As shown in Fig. 5, the electrostatic potential inside the nanochannel (-10 μm $< z < 10$ μm) varied according to the applied gate voltage. When the applied gate voltage was -2 V, a large potential drop occurred around $z = 8$ μm because of the depletion of the charge carrier. In contrast, a large potential drop occurred near $z = -8$ μm when $V_G = +2$ V. When V_G was 0.2964 V ($\approx$0.3 V), the electrostatic potential was linearly dropped through the whole nanochannel because the nanochannel was modulated to zero polarity. These results were important since the application of gate voltage can drop the strength of the electric field (a slope of electrostatic potentials) around the gate electrode so that one can possibly lower the translocation velocity of charged molecules through the gated nanochannel. Especially, since the gated regions of the nanochannels were transparent in our system, one can measure the speed in situ. Averaged concentration distributions were shown in Fig. 6 in which each section (divided by breaks) denoted nanochannel regions in the range of -8.1 μm $< z < -8$ μm, -5.07 μm $< z < -4.97$ μm, 4.97 μm $< z < 5.07$ μm, and 8 μm $< z < 8.1$ μm, respectively. As mentioned earlier, the depletion zone of the charge carrier was formed around $z = 8$ μm at $V_G = -2$ V, depicted as a white region in Fig. 6(a), and vice versa (Fig. 6(c) of $V_G = +2$ V). Because the nanochannel became zero polarity at $V_G = 0.2964$ V, the electric double layer cannot be built up and concentration distributions should be uniform as shown in Fig. 6(b). The flow fields depicted in Fig. 7(a) and (c) demonstrated that vortical flows were generated adjacent to the gated regions which were similar to the nanoporous membrane system.[35–38] As one can predict from the concentration distribution (Fig. 6), a strong vortex (thick arrows) was formed at the depletion zone, while a weak vortical
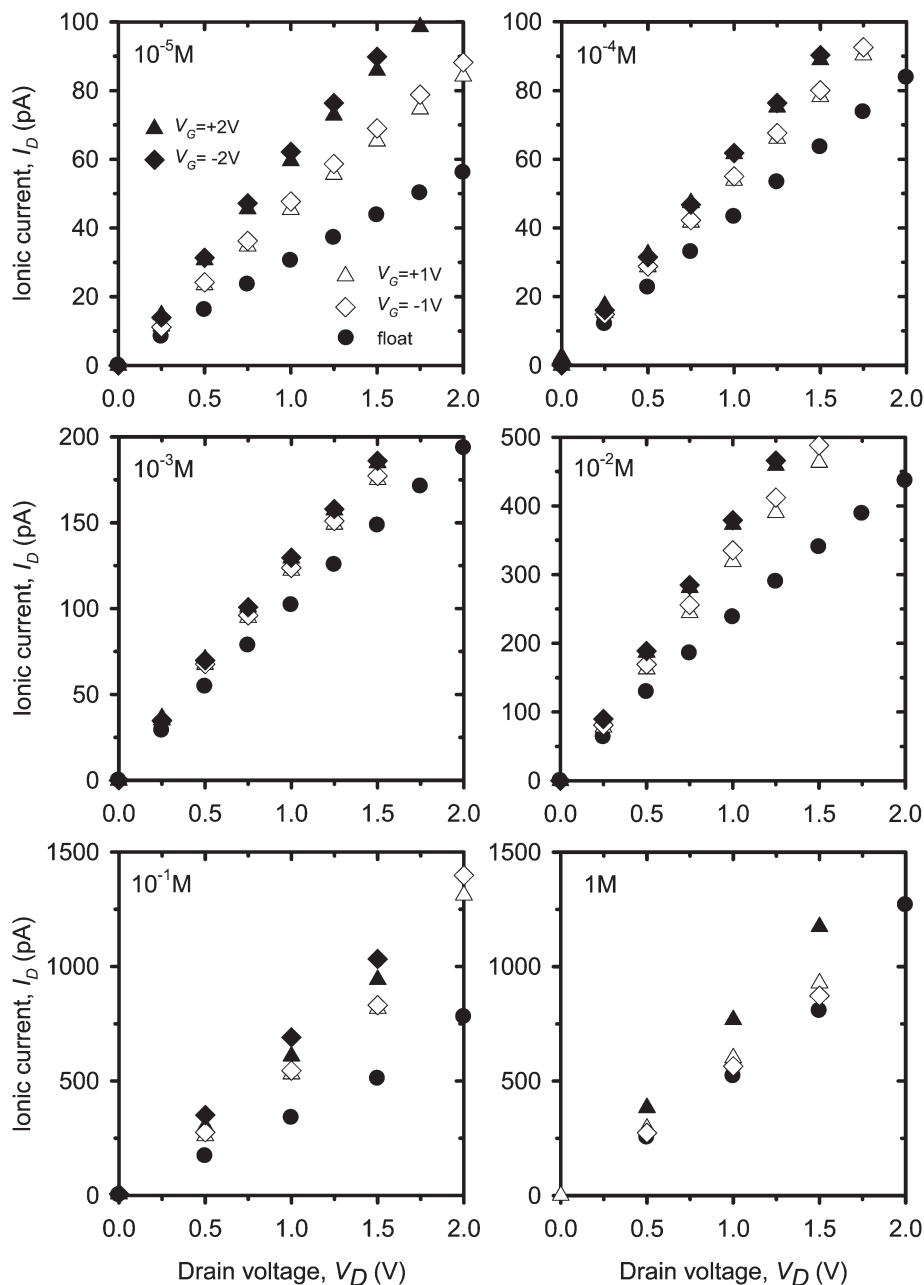
Fig. 4 Experimentally measured I_D–V_D characteristics in the concentration range of 10^{-5} M to 1 M. The conductance increased as a function of the absolute value (regardless of the polarity) of V_G.

motion (thin arrows) was observed at the other side. This was because the lower concentration led to higher electric field (Fig. 5) and strong electrokinetic flows. In Fig. 7(b), any electrokinetic flows were nonexistent because of the absence of the electric double layer. Consequently, electrokinetic fields such as concentration distributions and flow fields can be inverted by the applied gate voltage.

Ambipolar characteristics (I_D–V_G as a function of V_D): Numerical matching

In an ambipolar IFET device, I_D–V_G characteristics become V-shaped curves since the ionic current should be modulated

regardless of the polarity of gate voltage. On the contrary, a unipolar IFET has a diode behavior. The measured I_D–V_G characteristics were plotted in Fig. 8 for different electrolyte concentrations with numerical results. The measured I_D–V_G characteristics were ambipolar (V-shaped curve) since an inherently low surface charge density of Al_2O_3 (-1.5 mC m^{-2}) and higher capacitance of an all-around-gate structure ($\sim$5 times) than that of a planar-gate effectively reflected the gate polarity.

In a low (10^{-5} M–10^{-4} M) and an intermediate (10^{-3} M–10^{-2} M) concentration range, numerical results were well-matched with experimental data. For 10^{-5} M and 10^{-4} M, the extent of the ionic current modulation appeared in the same
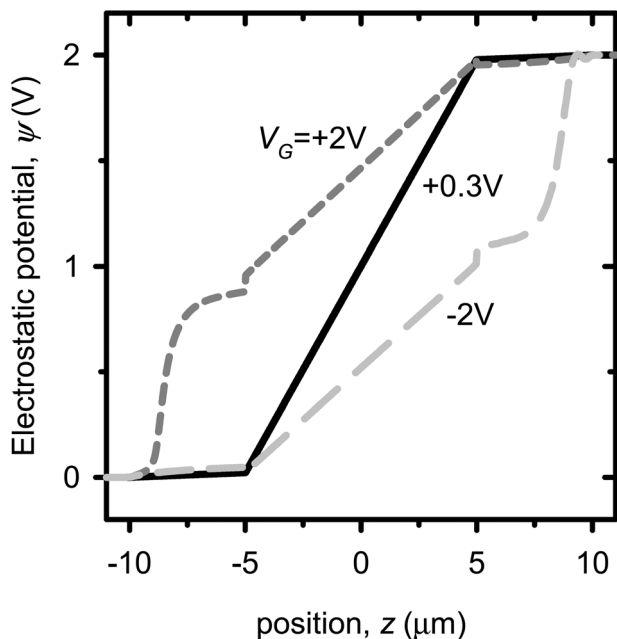
Fig. 5 Electrostatic potential as a function of z-axis at $V_D = +2$ V. The gated region lay between $z = -5$ μm and $z = 5$ μm.
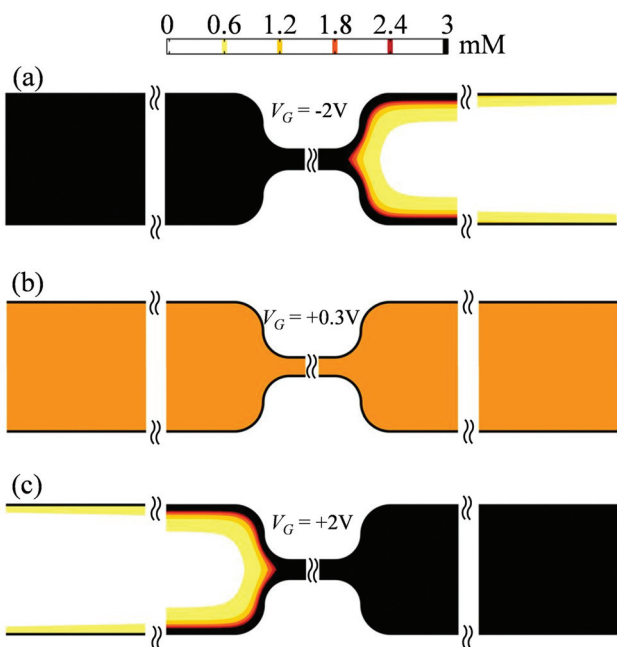

Fig. 6 Spatial distribution of averaged concentrations ($c_m = (c_K + c_{Cl})/2$). On these figures, the left side represents source (electrostatically ground) and the right side represents drain (2 V). Bulk concentration was fixed at 10^{-3} M. The applied gate voltage (V_G) was varied in each figure. Breaks denote nanochannel regions in the range of -8.1 μm $< z < -8$ μm, -5.07 μm $< z < -4.97$ μm, 4.97 μm $< z < 5.07$ μm, and 8 μm $< z < 8.1$ μm, respectively.
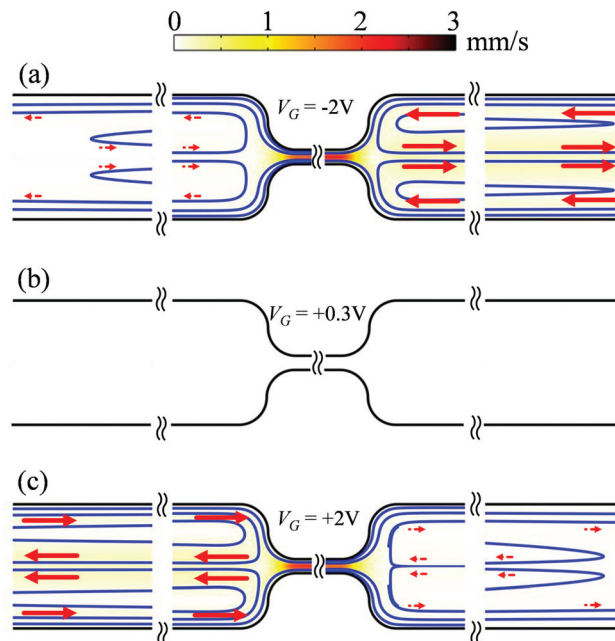

Fig. 7 Spatial distribution of electrokinetic flow fields. Voltage configuration and bulk concentration are the same as Fig. 6. Solid lines represent the stream lines and arrows represent flow directions and strengths.

of nanochannel rather than bulk property. Meanwhile, deviations between measured and numerical results occurred in the high concentration range (10^{-1} M–1 M). Higher bulk concentration gave larger deviation. Nevertheless, the measured I_D–V_G characteristics plotted in Fig. 8 were ambipolar. Consequently, more constraints in theoretical considerations would be needed to describe the ion transport at extremely high concentration.

The effects of fringing field and counter-ion condensation

We had adopted two additional constraints which were a fringing field effect and a counter-ion condensation to describe the ionic transportation through the partially-gated IFET. Compared to the Poisson–Nernst–Planck–Stokes formulation without any constraints (dashed line in Fig. 9), our modified formulation (solid line) was well-matched with experimental results. With a view point of the PNPS formulation without constraints, a positive gate voltage changed the polarity of the gated region only, and then, the nanochannel behaved as the npn nanofluidic transistor for negatively charged nanochannels. For the npn nanofluidic transistor, the application of a drain voltage could cause a reverse bias in one of the two pn junctions and hence the ionic current should be saturated,[39] leading to a unipolar behavior. Moreover, numerical results with negative gate voltage had non-negligible error compared to the experimental results. Therefore, the two constraints should be included in the PNPS formulation to correctly describe the ambipolar behavior of the presenting partially-gated IFET. The fringing fields which were generated in the non-gated region to satisfy $\nabla \times \mathbf{E} = \mathbf{0}$ could modulate the whole nanochannel and hence, the polarity of the entire nanochan-
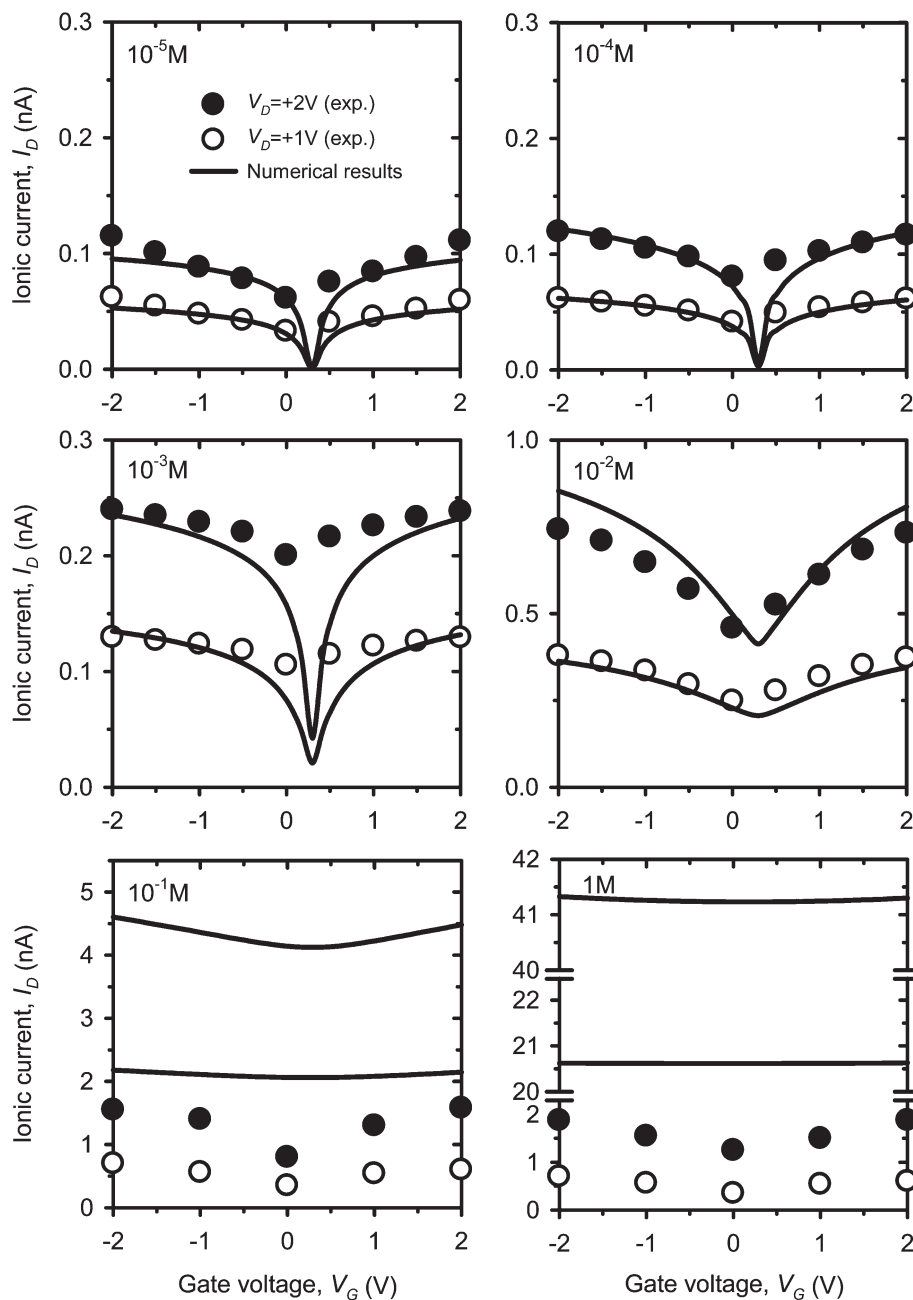
order of magnitude because those concentrations were in surface-charge-governed regime[10] where ion transport through the nanochannel is affected only by the surface charge density

Fig. 8 Experimental and numerical I_D–V_G at each electrolyte concentration. The "V" shape represents the ambipolar behavior.

nel became positive or negative depending on the gate voltage, while the gate voltage was applied only near the center of the nanochannel. Additionally, the condensed layer formed by counter-ions in the vicinity of the highly charged oxide/electrolyte interfaces let over-modulated surface charge drop down, so that the non-negligible numerical error at larger gate voltages was resolved. Therefore, fringing field effect and counter-ion condensation were essential constraints in IFET analysis.

Sensitive polarity inversion

The presenting IFET had lower threshold voltage to inverse the polarity of the nanochannel than previously reported

IFETs.[13,16] We defined the threshold voltage V_{th} as required gate voltage to regulate the zero-polarity of the nanochannel. When gate voltage was higher than V_{th}, the nanochannel had the positive polarity and *vice versa*. Using the condition of $\sigma_0 = 0$ at $V_G = V_{th}$, we derived the simplified equation for V_{th} related to oxide capacitance C_{ox} and inherent surface charge density σ_0 as

$$V_{th} = -\frac{\sigma_0}{C_{ox}} \tag{14}$$

Eqn (14) presented that IFET with higher oxide capacitance and lower inherent surface charge density had lower threshold voltage, leading to a sensitive polarity inversion. Since Al_2O_3
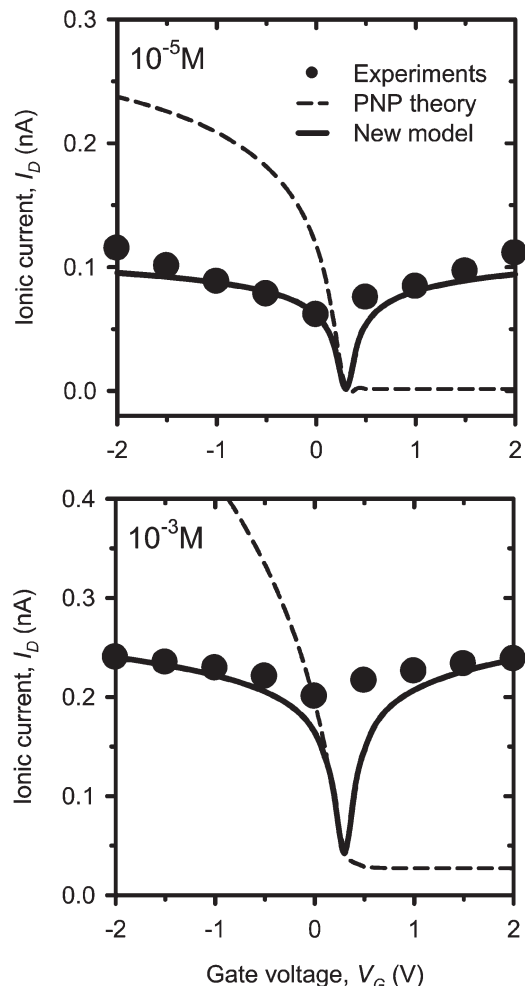
Fig. 9 Numerical matching of PNP theory and our new model with experimental values measured at $V_D = +2$ V. Bulk electrolyte concentration, c_0 (a) 10^{-5} M and (b) 10^{-3} M.
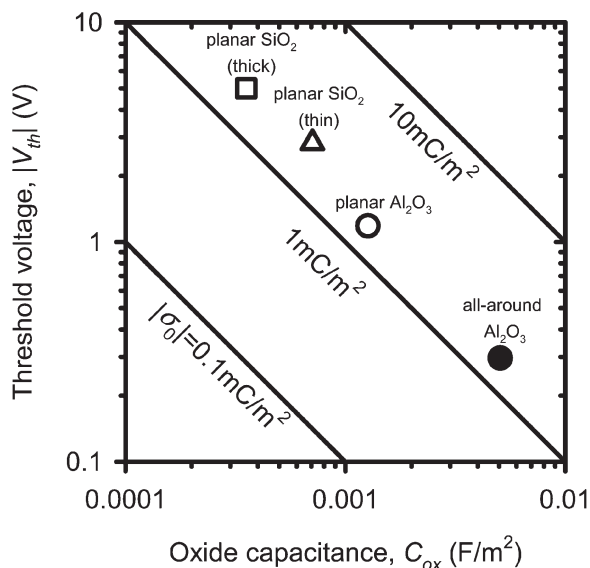

Fig. 10 Threshold voltages of various IFET devices. Planar-gate on thick SiO_2 (□) and planar-gate on thin SiO_2 (△) are from literature.[13,16]

used in this work had near-zero surface charge density (-1.5 mC m^{-2}) and capacitance of all-around-gate structure (5.06 mF m^{-2}) was 5 times higher than planar-gate structure, the threshold voltages of our device were calculated to be 0.2964 V from eqn (14) and 0.2967 V from numerical simulations which were superior to other IFET's V_{th}[13,16] as shown in Fig. 10.

Conclusion

In this work, we developed a transparent all-around-gated ionic field effect transistor (IFET) which has an ambipolar characteristic and can be operated at a wide range of electrolyte concentrations (10^{-5} M–1 M). Due to the relatively low oxide capacitance of a planar-gate structure and the inherently high surface charge density, a traditional IFET can only control the same polarity of charged species as the surface charge of the nanochannel. To enable the polarity-independent control, an all-around-gate structure was adapted to increase the efficiency of the gate effect compared to the planar-gate structure, and we used Al_2O_3 as the oxide layer which has lower surface charge density than SiO_2. As a result, ambipolar behavior was obtained by experiments and was validated by numerical simulations with a fringing field effect and a counter-ion condensation which had not been considered as major factors before. The numerical results demonstrated that the application of gate voltage can drop the strength of the electric field around the gated region so that one can possibly lower the translocation velocity of charged molecules through the nanochannel. In addition, the fabricated all-around-gated IFET had the lowest threshold voltage as required gate voltage to regulate the zero-polarity of the nanochannel. The use of this ambipolar IFET would provide significant advantages to cost-effective/on-demand/sensitive control of charged species such as ions (negative or positive), DNA (negative), RNA (negative), and proteins (negative or positive) regardless of their polarity which is important in a biomedical analysis such as biomolecule transport through nanochannels, medical diagnosis system, and point-of-care system, *etc.*

Acknowledgements

References

1 H. Daiguji, P. Yang, A. J. Szeri and A. Majumdar, *Nano Lett.*, 2004, **4**, 2315–2321.

2 W. Guo, L. Cao, J. Xia, F.-Q. Nie, W. Ma, J. Xue, Y. Song, D. Zhu, Y. Wang and L. Jiang, *Adv. Funct. Mater.*, 2010, **20**, 1339–1344.

3 M. Wanunu, W. Morrison, Y. Rabin, A. Y. Grosberg and A. Meller, *Nat. Nanotechnol.*, 2010, **5**, 160–165.

4 Y. Kim, K. S. Kim, K. L. Kounovsky, R. Chang, G. Y. Jung, J. J. dePablo, K. Jo and D. C. Schwartz, *Lab Chip*, 2011, **11**, 1721–1729.

5 T. C. Kinnaman, *Ecological Economics*, 2011, **70**, 1243–1249.

6 S. J. Kim, S. H. Ko, K. H. Kang and J. Han, *Nat. Nanotechnol.*, 2010, **5**, 297–301.

7 D. Fologea, J. Uplinger, B. Thomas, D. S. McNabb and J. Li, *Nano Lett.*, 2005, **5**, 1734–1737.

8 M. Utkur, C. Jeffrey, D. Valentin, A. Aleksei and T. Gregory, *Nanotechnology*, 2010, **21**, 395501.

9 M. Wanunu and A. Meller, *Nano Lett.*, 2007, **7**, 1580–1585.

10 D. Stein, M. Kruithof and C. Dekker, *Phys. Rev. Lett.*, 2004, **93**, 035901.

11 R. Karnik, K. Castelino, R. Fan, P. Yang and A. Majumdar, *Nano Lett.*, 2005, **5**, 1638–1642.

12 R. Karnik, R. Fan, M. Yue, D. Li, P. Yang and A. Majumdar, *Nano Lett.*, 2005, **5**, 943–948.

13 R. Fan, M. Yue, R. Karnik, A. Majumdar and P. Yang, *Phys. Rev. Lett.*, 2005, **95**, 086607.

14 R. Fan, S. Huh, R. Yan, J. Arnold and P. Yang, *Nat. Mater.*, 2008, **7**, 303–307.

15 U. Vermesh, J. W. Choi, O. Vermesh, R. Fan, J. Nagarah and J. R. Heath, *Nano Lett.*, 2009, **9**, 1315–1319.

16 W. Guan, R. Fan and M. A. Reed, *Nat. Commun.*, 2011, **2**, 506.

17 B. Kim, J. Heo, H. J. Kwon, S. J. Cho, J. Han, S. J. Kim and G. Lim, *ACS Nano*, 2013, **7**, 740–747.

18 J. Heo, H. J. Kwon, H. Jeon, B. Kim, S. J. Kim and G. Lim, *Nanoscale*, 2014, **6**, 9681–9688.

19 S. H. Tan, N. T. Nguyen, Y. C. Chua and T. G. Kang, *Biomicrofluidics*, 2010, **4**, 32204.

20 S.-W. Nam, M. J. Rooks, K.-B. Kim and S. M. Rossnagel, *Nano Lett.*, 2009, **9**, 2044–2048.

21 S.-W. Nam, M.-H. Lee, S.-H. Lee, D.-J. Lee, S. M. Rossnagel and K.-B. Kim, *Nano Lett.*, 2010, **10**, 3324–3329.

22 G. Pardon and W. van der Wijngaart, *Adv. Colloid Interface Sci.*, 2013, **199–200**, 78–94.

23 Z. Jiang and D. Stein, *Langmuir*, 2010, **26**, 8161–8173.

24 Z. Jiang and D. Stein, *Phys. Rev. E: Stat. Phys., Plasmas, Fluids, Relat. Interdiscip. Top.*, 2011, **83**, 031203.

25 L.-H. Yeh, S. Xue, S. W. Joo, S. Qian and J.-P. Hsu, *J. Phys. Chem. C*, 2012, **116**, 4209–4216.

26 C. Hughes, L.-H. Yeh and S. Qian, *J. Phys. Chem. C*, 2013, **117**, 9322–9331.

27 N. Hu, Y. Ai and S. Qian, *Sens. Actuators, B*, 2012, **161**, 1150–1167.

28 R. K. Wangsness, *Electromagnetic fields*, Wiley, 1986.

29 Y.-M. Lin, J. Appenzeller and P. Avouris, *Nano Lett.*, 2004, **4**, 947–950.

30 M. S. Kilic, M. Z. Bazant and A. Ajdari, *Phys. Rev. E: Stat. Phys., Plasmas, Fluids, Relat. Interdiscip. Top.*, 2007, **75**, 021502.

31 W. B. Russel, D. A. Saville and W. R. Schowalter, *Colloidal Dispersions*, Cambridge University Press, 1992.

32 G. S. Manning, *J. Phys. Chem. B*, 2007, **111**, 8554–8559.

33 R. M. M. Smeets, U. F. Keyser, D. Krapf, M.-Y. Wu, N. H. Dekker and C. Dekker, *Nano Lett.*, 2005, **6**, 89–95.

34 B. S. Reto, H. Jongyoon and R. Philippe, *Rev. Mod. Phys.*, 2008, **80**, 839.

35 I. Cho, G. Sung and S. J. Kim, *Nanoscale*, 2014, **6**, 4620–4626.

36 S. J. Kim, Y.-C. Wang, J. H. Lee, H. Jang and J. Han, *Phys. Rev. Lett.*, 2007, **99**, 044501.

37 E. V. Dydek, B. Zaltzman, I. Rubinstein, D. S. Deng, A. Mani and M. Z. Bazant, *Phys. Rev. Lett.*, 2011, **107**, 118301.

38 S. J. Kim, S. H. Ko, R. Kwak, J. D. Posner, K. H. Kang and J. Han, *Nanoscale*, 2012, **4**, 7406–7410.

39 L.-J. Cheng and L. J. Guo, *ACS Nano*, 2009, **3**, 575–584.